Quasielastic ^{12}C$(e, e'p)$ scattering up to $Q^2 = 14.2\,(GeV/c)^2$

D. Bhetuwal,[1] J. Matter,[2] H. Szumila-Vance,[3] C. Ayerbe Gayoso,[1, 10] M. L. Kabir,[1] D. Dutta,[1] R. Ent,[3] D. Abrams,[2] Z. Ahmed,[4] B. Aljawrneh,[5] S. Alsalmi,[6] R. Ambrose,[4] D. Androic,[7] W. Armstrong,[8] A. Asaturyan,[9] K. Assumin-Gyimah,[1] A. Bandari,[10] S. Basnet,[4] V. Berdnikov,[11] H. Bhatt,[1] D. Biswas,[12] W. U. Boeglin,[13] P. Bosted,[10] E. Brash,[14] M. H. S. Bukhari,[15] H. Chen,[2] J. P. Chen,[3] M. Chen,[2] E. M. Christy,[12] S. Covrig,[3] K. Craycraft,[16] S. Danagoulian,[5] D. Day,[2] M. Diefenthaler,[3] M. Dlamini,[17] J. Dunne,[1] B. Duran,[8] R. Evans,[4] H. Fenker,[3] N. Fomin,[16] E. Fuchey,[18] D. Gaskell,[3] T. N. Gautam,[12] F. A. Gonzalez,[19] J. O. Hansen,[3] F. Hauenstein,[20] A. V. Hernandez,[11] T. Horn,[11] G. M. Huber,[4] M. K. Jones,[3] S. Joosten,[21] A. Karki,[1] C. Keppel,[3] A. Khanal,[13] P. M. King,[17] E. Kinney,[22] H. S. Ko,[23] M. Kohl,[12] N. Lashley-Colthirst,[12] S. Li,[24] W. B. Li,[10] A. H. Liyanage,[12] D. Mack,[3] S. Malace,[3] P. Markowitz,[13] D. Meekins,[3] R. Michaels,[3] A. Mkrtchyan,[9] H. Mkrtchyan,[9] S.J. Nazeer,[12] S. Nanda,[1] G. Niculescu,[25] I. Niculescu,[25] D. Nguyen,[2] Nuruzzaman,[26] B. Pandey,[12] S. Park,[19] E. Pooser,[3] A. Puckett,[18] M. Rehfuss,[8] J. Reinhold,[13] N. Santiesteban,[24] B. Sawatzky,[3] G. R. Smith,[3] A. Sun,[27] V. Tadevosyan,[9] R. Trotta,[11] S. A. Wood,[3] C. Yero,[13] and J. Zhang[19]

(for the Hall C Collaboration)

[1] *Mississippi State University, Mississippi State, Mississippi 39762, USA*
[2] *University of Virginia, Charlottesville, Virginia 22903, USA*
[3] *Thomas Jefferson National Accelerator Facility, Newport News, Virginia 23606, USA*
[4] *University of Regina, Regina, Saskatchewan S4S 0A2, Canada*
[5] *North Carolina A & T State University, Greensboro, North Carolina 27411, USA*
[6] *Kent State University, Kent, Ohio 44240, USA*
[7] *University of Zagreb, Zagreb, Croatia*
[8] *Temple University, Philadelphia, Pennsylvania 19122, USA*
[9] *A.I. Alikhanyan National Science Laboratory (Yerevan Physics Institute), Yerevan 0036, Armenia*
[10] *The College of William & Mary, Williamsburg, Virginia 23185, USA*
[11] *Catholic University of America, Washington, DC 20064, USA*
[12] *Hampton University, Hampton, Virginia 23669, USA*
[13] *Florida International University, University Park, Florida 33199, USA*
[14] *Christopher Newport University, Newport News, Virginia 23606, USA*
[15] *Jazan University, Jazan 45142, Saudi Arabia*
[16] *University of Tennessee, Knoxville, Tennessee 37996, USA*
[17] *Ohio University, Athens, Ohio 45701, USA*
[18] *University of Connecticut, Storrs, Connecticut 06269, USA*
[19] *Stony Brook University, Stony Brook, New York 11794, USA*
[20] *Old Dominion University, Norfolk, Virginia 23529, USA*
[21] *Argonne National Laboratory, Lemont, Illinois 60439, USA*
[22] *University of Colorado Boulder, Boulder, Colorado 80309, USA*
[23] *Institut de Physique Nucleaire, Orsay, France*
[24] *University of New Hampshire, Durham, New Hampshire 03824, USA*
[25] *James Madison University, Harrisonburg, Virginia 22807, USA*
[26] *Rutgers University, New Brunswick, New Jersey 08854, USA*
[27] *Carnegie Mellon University, Pittsburgh, Pennsylvania 15213, USA*

(Dated: April 12, 2022)

Quasi-elastic scattering on ^{12}C$(e, e'p)$ was measured in Hall C at Jefferson Lab for space-like 4-momentum transfer squared Q^2 in the range of 8–14.2 (GeV/c)^2 with proton momenta up to 8.3 GeV/c. The experiment was carried out in the upgraded Hall C at Jefferson Lab. It used the existing high momentum spectrometer and the new super-high momentum spectrometer to detect the scattered electrons and protons in coincidence. The nuclear transparency was extracted as the ratio of the measured yield to the yield calculated in the plane wave impulse approximation. Additionally, the transparency of the $1s_{1/2}$ and $1p_{3/2}$ shell protons in ^{12}C was extracted, and the asymmetry of the missing momentum distribution was examined for hints of CT effects. All of these results were found to be consistent with traditional nuclear physics and inconsistent with the quantum chromodynamics predictions for the onset of Color Transparency.

I. INTRODUCTION

The $(e, e'p)$ reaction, also known as a proton-knockout reaction, is a fundamental tool for studying the propagation of nucleons in the nuclear medium. Specifically, the weak electromagnetic probe is able to sample the full nuclear volume (as compared to hadronic probes). The kinematics of the reaction are well-defined by the electron, and the momentum transferred can be independently varied from the energy transferred in the reaction. This enables a clean selection of parameter space for studying the propagation of the knocked-out proton through the nuclear medium and its final state interactions (FSI). The sensitivity to FSI makes quasi-elastic scattering an ideal probe of the phenomenon of Color Transparency (CT) predicted by Quantum Chromodynamics (QCD).

Theoretical calculations in the quark-gluon framework of QCD predict that in exclusive processes at large four-momentum transfer squared, Q^2, the FSI between the hadrons and the nuclear medium are reduced or suppressed. In the case of quasi-elastic electron scattering, only the FSI of the knocked-out proton are relevant. The concept of CT was first proposed by Mueller and Brodsky [1, 2] in the context of perturbative QCD but was later shown to arise in nonperturbative models too. An analogue of CT can be seen in Quantum Electrodynamics; an e^+e^- pair has a small interaction cross section near the production point acting as a dipole (neutral charge) instead of as isolated charged particles [3, 4].

The onset of CT requires the following conditions:

- Squeezing: at sufficiently high Q^2 the preferential selection of a small configuration of quarks, sometimes referred to as a point-like configuration (PLC)
- Freezing: the PLC ejected at a high momentum maintains its small size over a distance comparable to or greater than the nuclear radius
- The in-medium interaction of the PLC as a color-neutral object is proportional to the square of its transverse radius and thus, has reduced interaction with the nuclear medium as it transits the nucleus

Squeezing is experimentally controlled through the choice of the momentum transfer whereas freezing is described by the energy transfer of the reaction. It is the interplay between squeezing and freezing that is important to observing the onset of CT.

The onset of CT has been observed in mesons [5–10], whereas its onset in baryons remains uncertain with experimental results to date leading to ambiguous conclusions. For instance, the *pp* scattering experiments at Brookhaven National Laboratory (BNL) [11–13] claimed to have initially found the onset of CT in protons, but the full results were inconsistent with a CT-only description. The BNL results have since been better explained with descriptions that include nuclear filtering [14] or exotic multi-quark final states [15].

The nuclear transparency is the common observable for experiments searching for the onset of CT, and it is described as $T = \sigma_A/A\sigma_0$, or the ratio of the nuclear cross section per nucleon, σ_A/A, to the cross section for a free nucleon, σ_0. Traditional Glauber multiple scattering theory [16] predicts that T is constant as Q^2 increases. It is specific to the qualities of QCD that one may predict the reduction of inital/final state interactions, characterized as CT, subsequently resulting in an increase in the nuclear transparency with increasing Q^2.

All previous measurements of the momentum dependence of the proton transparency in quasi-elastic electron scattering have been consistent with the Glauber prediction, indicating no deviation with increasing momentum transfer. The most recent experiment, E1206107 - The Search for Color Transparency at 12 GeV [17], took place at Jefferson Lab (JLab) and extended the range of Q^2 up to 14.2 $(\mathrm{GeV}/c)^2$, the highest Q^2 studied to date for this reaction. The results indicate no signal consistent with the onset of CT [18] in this range. In this article we elaborate on the experimental details and report additional results on proton transparency separated by nuclear shells and the asymmetry of the missing momentum distribution.

II. EXPERIMENTAL SET-UP

This experiment was the first to be completed in Hall C after the beam energy upgrade of the continuous electron beam accelerator facility (CEBAF). The focus of this experiment was to study the semi-exclusive quasi-elastic $^{12}C(e,e'p)$ reaction, the knockout of a proton by an incident electron in a Carbon target.

The experiment was designed to overlap with the existing $Q^2 = 8.1\,(\mathrm{GeV}/c)^2$ data point from the highest previous Q^2 $A(e,e'p)$ experiment at JLab [19] in order to help validate the results. The experiment measured nuclear transparency covering the range of outgoing proton momenta, (p'), of the BNL $A(p,2p)$ experiment where a rise in nuclear transparency had been previously reported [20]. The use of the electron beam as opposed to a hadronic probe is ideal for such measurements as it avoids the ambiguity that arises from the reduction of flux of the probe when extracting the nuclear transparency. This experiment extended the Q^2 and p' range to the highest achieved in quasi-elastic proton knockout to date.

A. Beam

The experiment used the continuous wave (CW) electron beam with energies of 6.4 and 10.6 GeV and beam currents of $10 - 65\,\mu$A. The electron beam is accelerated using superconducting radio frequency cavities. The duty factor of the beam is $\sim 100\%$ and consists of pulses occurring at a frequency of 1497 MHz with an energy spread of $\pm 0.025\%$. The beam is sequentially delivered to all four experimental halls, allowing each experimental hall to operate simultaneously with different beam current and energy [21]. The beam delivered to Hall C was every third pulse of the beam with a frequency of 499 MHz. The beam energy was determined with an uncertainty of 0.1% by measuring the bend angle of the beam on its way into Hall C while traversing a set of magnets with precisely known field integrals.

B. Target

A 10 cm long (726 mg/cm^2) liquid hydrogen target was used for normalization to the elementary ep scattering process. Two aluminum foils placed 10 cm apart were used to monitor the background from the aluminum end caps of the hydrogen target cell. The main production target was a carbon foil of 4.9% radiation lengths (rl), while a second carbon foil of 1.5% rl was used for systematic studies. The thicknesses of the foils were measured to better than 0.5%. The beam incident on the liquid hydrogen target was rastered over a 2×2 mm^2 area to suppress density variations from localized boiling.

C. Spectrometers

Hall C has two magnetic spectrometers, the High Momentum Spectrometer (HMS), which has been the main spectrometer in Hall C during the JLab 6 GeV era, and the new Super High Momentum Spectrometer (SHMS).

The HMS which served as the electron detection arm consists of three quadrupoles (Q) and a dipole (D) magnet arranged in $Q_1Q_2Q_3D$ configuration capable of bending the scattered particles into the detector stack at an angle of 25°. Details about the HMS can be found in the Ref. [22].

The SHMS which served as the proton detection arm has an extra dipole magnet known as the horizontal bender (HB) that bends the scattered particles horizontally by 3° from the beam line before reaching the first quadrupole. The configuration after the HB is the same as the HMS with three quadrupoles and the dipole magnet. The final dipole bends the particles into the detector stack by 18.4°. The characteristics of both spectrometers are summarized in the table I.

The scattered electrons were detected in the HMS in coincidence with the knocked-out protons detected in the SHMS. The SHMS central angle was chosen to detect protons along the electron three-momentum transfer, $\vec{q}$. The kinematics for data taking were chosen keeping in mind to minimize the effects of FSI. The measured final state proton momentum ranged from $5.030 - 8.352\,\mathrm{GeV}/c$. The electron beam energy was 6.4 GeV for the $Q^2 = 8.0\,(\mathrm{GeV}/c)^2$ setting and 10.6 GeV for the rest.

D. Detectors

Each spectrometer in Hall C has a set of detectors stacked in the detector hut at the end of the spectrometer. Both spectrometers are equipped with a four-plane segmented hodoscope for triggering, time-of-flight measurements, and coarse tracking; multi-wire drift chambers for precision tracking; and a combination of a lead glass calorimeter and threshold Čerenkov counters for particle identification.

TABLE I. Hall C Spectrometers characteristics

	HMS [23]	**SHMS** [24]
Momentum acceptance $\Delta p/p$ (%)	±10	-10 to +22
Solid angle acceptance Ω (msr)	8.1	>4
Momentum resolution (%)	0.1-0.15	0.03-0.08
Central momentum (p) (GeV/c)	0.4-7.4	2-11
Scattering angle (θ) (°)	10.5-90	5.5-40
Target resolution (ytar) (cm)	0.3	0.1-0.3
Maximum event rate (kHz)	2	10

The HMS lead glass calorimeter and gas Čerenkov counter allow e/π^- separation. The Čerenkov counter was filled with C_4F_8O at 0.45 atm corresponding to an index of refraction of n = 1.0006165 and a momentum threshold of 0.15 GeV/c for electrons and 3.97 GeV/c for pions. The HMS Čerenkov provides sufficient electron/pion discrimination for the highest and lowest kinematic points, but additional information from the calorimeter was required for the middle two kinematic points.

The SHMS is equipped with a Noble Gas Čerenkov that was used as a veto to reject pions. The Noble Gas Čerenkov counter was filled with CO_2 at 1.0 atm corresponding to an index of refraction of n = 1.000449 with a momentum threshold of 4.66 GeV/c for pions and 31.1 GeV/c for protons.

The HMS and SHMS each contain pairs of drift chambers that give the hit position information of charged particles as well as a drift time for each hit that was used for track reconstruction. Two pairs of X-Y scintillator hodoscope planes in the HMS and SHMS formed the trigger for the data acquisition (DAQ). The fast timing response of the scintillators also measured the particle's time of flight (TOF). By using the particle track information from the drift chambers in combination with the timing information, the velocity of the particle (β) was determined and used for particle identification.

E. Kinematics

Four kinematic settings were used in this experiment covering a range of Q^2 = 8–14.2 (GeV/c)^2 and proton momenta from 5–8.3 GeV/c. The lowest Q^2 setting was directly comparable and overlapped with previous results [19]. The kinematics for this experiment are shown in Table II.

TABLE II. Kinematic settings of the experiment, E_b is the electron beam energy, p_p and p_θ correspond to the central momentum and angle of the proton spectrometer while e_p and e_θ correspond to the central momentum and angle of the electron spectrometer, and ϵ is the degree of virtual photon polarization that measures the polarization of the virtual photon exchanged by the electron scattered at an angle e_θ.

$\mathbf{E}_b$ (GeV)	$\boldsymbol{Q^2}$ $(\mathrm{GeV}/c)^2$	$\mathbf{p}_\theta$ (deg)	$\mathbf{p}_p$ (GeV/c)	$\mathbf{e}_\theta$ (deg)	$\mathbf{e}_p$ (GeV/c)	ϵ
6.4	8.0	17.1	5.030	45.1	2.125	0.47
10.6	9.4	21.6	5.830	23.2	5.481	0.76
10.6	11.4	17.8	6.882	28.5	4.451	0.64
10.6	14.2	12.8	8.352	39.3	2.970	0.44

III. DATA ANALYSIS

A. Calibrations

The experiment used drift chambers, hodoscopes, Čerenkov detectors and calorimeters in both the HMS and SHMS. Each system was calibrated in order to match the signal arrival time for the individual scintillator elements and to match the gains of the calorimeter and Čerenkov signals. A few selected distributions from those calibrations are shown in the Fig. 1.

The drift chamber calibration requires determining the start time offsets (t_0) on a per-wire/per-card basis. These t_0 offsets are the corrections by which the drift time spectrum of each wire/card must be shifted to ensure the start of the drift time distribution at 0 ns. For well calibrated chambers, the distribution of drift distances (the distance an ionized particle has to traverse across a cell) must be flat and the residual (the difference between the final track position and the hit location from an individual plane) distributions should have widths $\leq 250\mu$m, corresponding to the tracking resolution for both the HMS and SHMS.

The calibration of the calorimeters converts the digitized detector signal (i.e. output of the analog-to-digital converters (ADC)) into the total energy deposited by the particle. The calibration is obtained using high statistics electron beam data by examining the normalized track energy, defined as the energy deposited by the electron in the shower/preshower blocks in the calorimeter divided by the particle's track momentum. For a well calibrated calorimeter, this ratio peaks at unity with the minimum width possible and is independent of the relative momentum (δ) and the position of the hit.

The hodoscopes provide the fast triggering and precise timing for the experiment. The timing calibration provides the timing correction value and is accomplished by determining the TOF offset and time walk corrections for each hodoscope paddle relative to a reference paddle in the stack. With the known offsets, the β calculated from the TOF is peaked at unity independent of relative momentum, δ, and the hit position. For more discussion on the detector calibration, see Ref. [25].

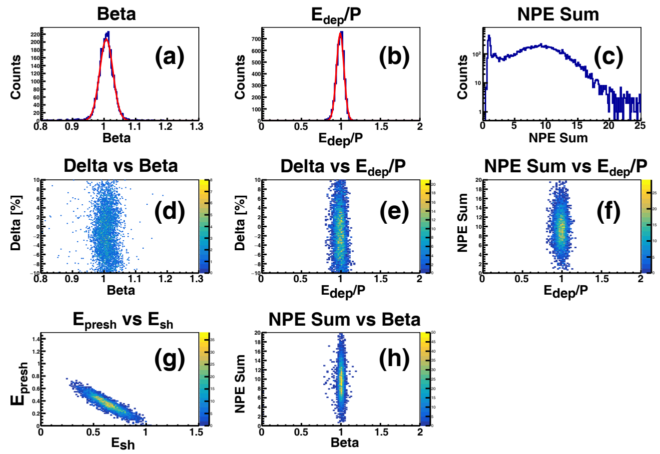

FIG. 1. Calibration plots from hodoscopes, shower, preshower and calorimeter. (a), β. (b), $\mathrm{E_{tot}}$/P (total energy deposited normalized by the central momentum). (c), number of photoelectrons sum. (d), Δp /p vs β. (e), Δp /p vs $\mathrm{E_{tot}}$/P. (f), number of photoelectrons sum vs $\mathrm{E_{tot}}$/P. (g), Shower Energy vs Preshower Energy. (h), number of photoelectrons sum vs β.

B. Beam charge accounting

The electron beam charge accounting setup in Hall C consists of several RF cavities used as Beam Current Monitors (BCMs) and an Unser parametric current transformer (PCT) which is a parametric direct current transformer having an extremely stable gain. The Unser is calibrated by injecting a known current into a calibration wire. The rate of the Unser output signal is recorded against the known current. The slope of this linear relationship gives the gain. However, the Unser suffers from large drifts in the zero current offset requiring periodic re-calibration during experimental running. Thus, the Unser current is used as a high precision reference for the BCMs after removing the unstable zero offset. The BCMs are stainless steel cylindrical waveguides that are tuned to the beam's frequency (1497 MHz) and are designed for stable, low noise, non-destructive beam current measurements. As the electron beam passes through the cavity on its way to the target, it induces currents in the cavity that are proportional to the intensity of the electron beam passing through it. The BCM cavities are used to measure current during the experiment due to their high stability. The total accumulated beam charge was determined with $\approx 1\%$ uncertainty.

C. Deadtime accounting

In order to calculate the experimental yield, it is necessary to consider those events arriving while the data acquisition (DAQ) is busy. This busy time, or dead time, originates from two main sources: the electronic dead time which is the period when the trigger hardware is busy, and the computer dead time which is due to the finite time the DAQ computer needs to process and record events. It is worthy to note that the dead time is most often quoted in terms of the fraction of time the DAQ system is busy.

In this experiment the DAQ had a rate-dependent computer live time (CLT) which was calculated from the ratio of recorded (accepted) physics triggers and the total physics triggers. To measure the dead time due to all electronics module in the DAQ system, an Electronics Dead Time Measurement (EDTM) trigger is inserted into the trigger logic. The EDTM is a real trigger and had a small frequency (~ 3 Hz) to minimize the probability of blocking actual physics triggers. The EDTM pulses fire every trigger in the system and are used to estimate of the Total Live Time (TLT), which is calculated from the ratio of the number of EDTM triggers that are accepted by the DAQ and the total number of pulses counted by the EDTM scaler.

The EDTM trigger was available during the experiment except for the lowest Q^2 of 8 $(\mathrm{GeV}/c)^2$ setting. For this setting, we extrapolated from kinematics that had similar rates and a known dead time. For more discussion on the live time calculations, see Refs. [26, 27].

D. Spectrometer optimizations

The experiment was one of the first experiments to use the newly built SHMS to detect protons. The experiment used the SHMS over a wide range of central momenta and angles and measured the highest momentum protons in JLab (8.3 GeV/c), to date. Significant effort was made at the start of this experiment to characterize and optimize the SHMS optics. The fields for each of the magnets in the SHMS were modeled with the static field analysis code TOSCA [28]. The Q_2 and Q_3 quadrupole magnets are nearly identical and have no saturation implemented in their models. The HB is characterized by saturation above approximately 4 GeV/c. The model for the HB magnet was compared against field mapping measurements along the central axis. The Q_1 magnet was also determined to have some saturation effects above approximately 7.5 GeV/c, and these effects were measured only by measuring the central field values of the magnet versus the current to validate the more detailed TOSCA models. The magnets in the SHMS were set by their currents that were measured in the magnet and compared with TOSCA models. The HMS is generally well-understood through its extensive use in Hall C. The HMS analyzing dipole differs from that of the SHMS, as approximately half of its field is generated by the surrounding iron yoke of the magnet. As such, the HMS dipole is characterized by a larger settling time of the magnet. The quadrupole magnets in the HMS were set using the same current to field ratios established and verified during previous use. The HMS spectrometer dipole is set by field regulation based on field values both measured and verified by TOSCA models. The well understood response of the HMS optics was further verified through hydrogen elastic cross-section measurements.

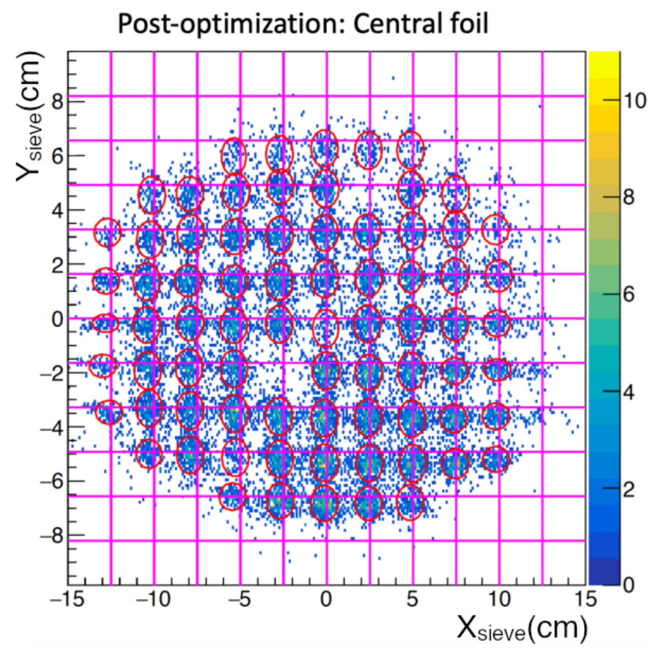

FIG. 2. Reconstructed sieve aperture pattern for the central target foil in the SHMS. The central hole is half diameter compared to the other sieve holes, and two empty sieve positions are observed to be consistent with sieve holes that are blocked.

Tracks reconstructed from the drift chamber hits provide the vertical (horizontal) position $x(y)$ and vertical (horizontal) angles $x' = \frac{dx}{dz}(y' = \frac{dy}{dz})$ of the particles at the focal plane. The positions and angles at the focal plane can be precisely mapped back to the position and angles at the interaction point in the target through a set of polynomial transformations. An initial set of coefficients for these transformations was generated using the COSY program [29], which is a code for the simulation, analysis and design of particle optical system, and is based on differential algebraic methods. The mapping was further optimized using dedicated data collected with a set of special purpose array of fixed apertures (sieve slits) and multi-foil extended carbon target. The optics optimization data for both the HMS and SHMS were collected using the electron beam at an incident energy of 6.4 GeV/c with central momenta of 2, 3, and 3.2 GeV/c. Two targets were used to collect this data: a three-foil target with carbon foils at ± 10 cm and 0 cm, and a two-foil target with carbon foils at ±5 cm along the beam direction (z). The sieve slits were placed downstream of the target in front of the first quadrupole magnet in each spectrometer arm. The events that passed through the sieve holes were used to optimize the reconstruction map using a singular value decomposition (SVD) algorithm [30] to fine tune the coefficients generated from the COSY models and to accurately reproduce the positions and angles of the apertures. The optimized sieve aperture pattern for the SHMS is shown in Fig. 2.

The true sieve hole positions are shown by the grid intersections in Fig. 2, and the events associated with those sieve holes are indicated by the red ellipse around those positions. The optimized mapping was valid up to central momenta of 3.2 GeV/c. There were some anticipated magnetic saturation effects in the horizontal bender and Q1 magnets when the magnets were set for higher central momentum. These offsets were verified by observing the location of the waist of the focal plane distribution at these settings. The performance of the magnets at high central momenta was fine-tuned using elastic hydrogen data at each kinematic setting.

E. Detector Efficiency

Detector efficiency is defined as the ratio of the number of particles that produced measurable signal to the number of particles that traversed the detector and should have produced a signal in the detector under consideration. The calorimeter, Čerenkov and hodoscope efficiencies for the ^1H and ^{12}C targets were determined to be ∼99% in both HMS and SHMS spectrometers. Tracking efficiency in the HMS spectrometer was found to be >99%, and in the SHMS spectrometer it ranged from 93% − 97%. A series of dedicated single arm runs were taken on the ^{12}C target to measure the charge normalized yield as a function of the beam current (also known as a luminosity scan). For a ^{12}C target it is expected that the corrected charge normalized yield should be independent of beam current. The uncertainties due to the live time correction, and the detector and trigger inefficiencies were determined from a set of luminosity scans performed with each spectrometer at the beginning and at the end of the experiment. The charge normalized yield from these scans for each spectrometer was found to be independent of the beam current within statistical uncertainties, and the average variation in the normalized yield vs beam current was recorded as the systematic uncertainty, which we determined to be 0.5%.

F. Target Boiling

The density of the 10 cm liquid ^1H target can vary with the incident electron beam current which is known as beam boiling effect (at a microscopic level as the e^- beam interacts with the target, the number of target atoms on a local unit volume changes as the beam deposits power on it), and the experimental yield was corrected for this effect. A series of dedicated single arm runs at different beam currents were taken to study the boiling effect in the ^1H target before and after collecting the production data. The charge normalized yield was determined as a function of the beam current. A linear fit of the reduction in yield as a function of the increasing beam currents was used to obtain a target boiling correction to the experimental yield. The correction was determined to be 2.6% at the highest beam current used, which was 65 μA.

G. Simulation of the Experiment

1. Acceptance

The acceptance of the spectrometers was studied using the SIMC simulation tool [31]. SIMC includes models generated by COSY for the spectrometer optics that transport the charged particles through the magnetic fields of all magnets in each spectrometer arm. The effects of multiple scattering and ionization energy loss for particles passing through all materials and apertures is included in the forward transport simulation. A second set of maps generated by COSY are used to relate the particle tracks at the focal plane of the spectrometer to the angles, momentum, and position at the interaction vertex in the target. Simulated events are weighted by the calculated Plane Wave Impulse Approximation (PWIA) cross-section, radiative correction, and Coulomb correction. The PWIA cross-section was calculated using the De Forest [32] σ_{cc1} prescription for the off-shell electron-proton cross-section and an independent particle shell model (IPSM) spectral function for the target nucleus [33].

The reconstructed angles and momentum at the target from hydrogen elastic scattering are compared between data and simulation as shown in Fig. 3. The exclusive nature of elastic scattering was used to better validate the spectrometer optics and to ultimately quantify how well the true acceptance is modeled. As a typical example, the comparisons between data and SIMC for the $Q^2 = 8\,(\mathrm{GeV}/c)^2$ kinematics are shown in Fig. 3.

The yield from the SIMC simulation was obtained by accounting for the experimental luminosity, the phase space volume, and the number of events generated.

2. Spectral functions

The PWIA $(e, e'p)$ cross-section can be written as the product of ep cross-section (σ_{ep}) and a probability function $S(E_s, \mathbf{p}_m)$, also known as the spectral function:

$$\frac{d^6\sigma}{dE_{e'}d\Omega_{e'}dE_{p'}d\Omega p'} = p' E_{p'} \sigma_{ep} S(E_s, \mathbf{p}_m). \quad (1)$$

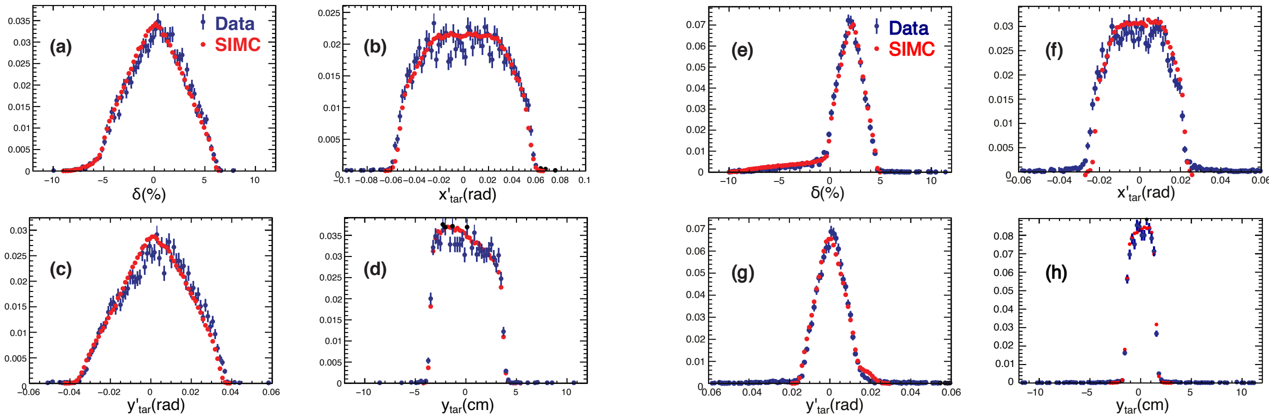

FIG. 3. The reconstructed angles at the target and momentum compared between data (blue) and simulated spectra (red). Panels (a) - (d) show the momentum resolution δ (a), vertical angle (x'_{tar}) (b), horizontal angle (y'_{tar}) (c) and reconstructed horizontal position (y_{tar}) for the electrons in the HMS. Panels (e) - (g) show the momentum resolution δ (e), vertical (f), horizontal angle (g), and reconstructed horizontal position (h) for the proton in the SHMS.

The spectral function represents the probability of measuring a proton with missing (initial) momentum $\mathbf{p}_m$ and separation energy E_s (experimentally measured as missing energy, E_m). The two quantities $\vec{p}_m$ and E_m are defined as:

$$\vec{p}_m = \vec{p}\,' - \vec{q}, \quad \text{and} \quad E_m = \nu - T_{nuc} - T_b, \qquad (2)$$

where $\vec{p}\,'$ is the measured outgoing proton momentum, $\vec{q}$ and ν are the momentum and energy transferred between the incident and scattered electron respectively, T_{nuc} is the kinetic energy of the struck proton and T_b is the kinetic energy of the (undetected) recoiling $A-1$ system. In our experiment, we work in parallel kinematics such that $\vec{p}$ is parallel to $\vec{q}$.

In the IPSM, the nucleons are treated as free particles, and the spectral function has a different probability for each shell. However, it neglects that the nucleons are bound and hence off-shell. This means $E^2 \neq \vec{p}^{\,2} + M^2$, in general. The electron scattering cross-section depends on the proton's initial energy, which yields two alternatives, either $E = M - E_s$ or $E^2 = \vec{p}^{\,2} + M^2$. The choice of assumptions results in differing off-shell cross-section prescriptions.

The two often used off-shell prescription models are De Forest σ_{cc1} and σ_{cc2} [34, 35]. The subscript cc refers to the current conservation, and obeys $\vec{q}\,\vec{J} = \nu\rho$, with $\vec{q}$ the virtual photon three momentum, $\vec{J}$ the nuclear current density, ν is the virtual photon energy, defined before, and ρ the nuclear charge density. This experiment uses the De Forest σ_{cc1} prescription for the off-shell cross-section. The full computed cross-section model for all kinematics was observed to be insensitive to the choice of off-shell prescription (between σ_{cc1} and σ_{cc2}) at $< 0.1\%$. The IPSM spectral functions used in previous experiments [19, 33, 36, 37] were employed in this experiment.

3. *Radiative corrections*

The radiative effect in the electron scattering reaction is a result of the deceleration of the charged particle in the presence of the Coulomb field of the nucleus. The resulting radiation from such deceleration of the electron is called Bremsstrahlung radiation. The radiative effect modifies the cross-section of the process and the kinematics (such as energy, momentum, angle) of the electron. The theoretical calculations do not take these effects into account most of the time, even though this is a real physical effect. Thus, the theoretical models must be corrected prior to comparison with the experimental data. The radiative corrections in SIMC were based on the formalism developed by Mo and Tsai [38] and adapted for coincident $(e, e'p)$ reactions [39].

Figure 4 is the hydrogen missing energy distribution for $Q^2 = 8\,(\mathrm{GeV}/c)^2$ comparing data (blue) and Monte Carlo showing the data cut off region at 65 MeV. Similarly, Figure 5 is the carbon missing energy plot for $Q^2 = 8\,(\mathrm{GeV}/c)^2$ comparing data (blue) and Monte Carlo, showing the data cut off region at 80 MeV. In both Figures, the black distributions show that the Monte Carlo without radiative corrections applied is more sharply peaked, in contrast to the red distributions showing that the Monte Carlo inclusive of radiative corrections is broadened as it loses its energy in the form of radiated photons, which is seen in the tails at high missing energy. In the high missing energy regime, the data are well-described by the simulation that includes the radiative effects.

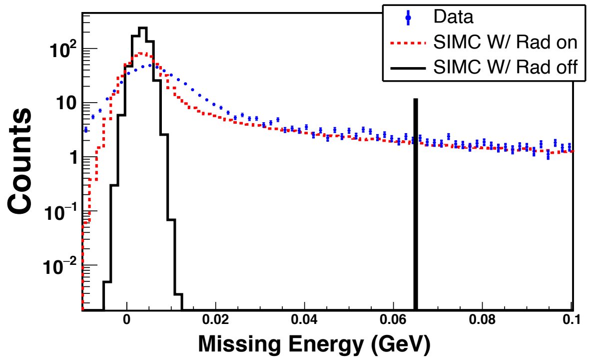

FIG. 4. Hydrogen missing energy plot for $Q^2\!=\!8\,(\mathrm{GeV}/c)^2$ comparing Data (blue dots) and Monte Carlo with (red dashed line) and without (black line) radiative correction. The vertical black line at 65 MeV indicates E_{miss} data cut for hydrogen.

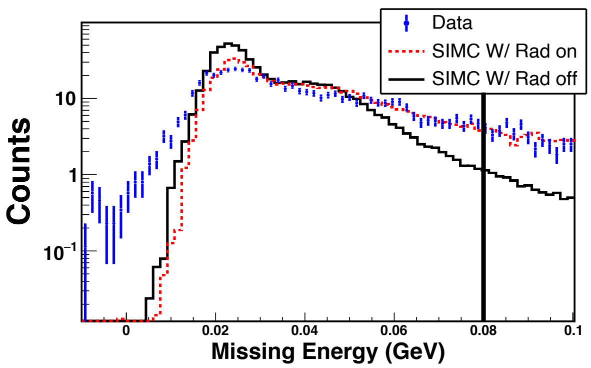

FIG. 5. Carbon missing energy plot for $Q^2\!=\!8\,(\mathrm{GeV}/c)^2$ comparing Data (blue dots) and Monte Carlo with (red dashed line) and without (black line) radiative correction. The vertical black line at 80 MeV indicates E_{miss} data cut for carbon in the final charge normalized yield calculation in E1206107.

H. Proton Absorption

Because protons are strongly interacting particles, they may undergo a nuclear reaction as they pass through the materials of the SHMS before forming a trigger. The proton absorption, A, is defined as the fraction of protons that fail to form a trigger due to their interaction with the matter before reaching the detectors. An estimation of the absorption is obtained by considering the proton's mean free path in the materials along its trajectory through the SHMS. The mean free path is estimated from:

- the nuclear collision length: $\lambda_T = \sum_i A_i/(N_A \rho_i \sigma_{tot_i})$ where N_A is Avogadro's number, A_i the atomic weight, ρ_i the mass density and $\sigma_{tot,i}$ the total nuclear cross-section of the $i$component of the material composition.
- the nuclear interaction length: λ_I, which is similarly defined as the nuclear collision length but subtracts the elastic and quasi-elastic cross-sections from $\sigma_{tot,i}$.

Because the elastic cross-section is peaked in the forward direction, thus removing only a few protons from the spectrometer's acceptance, we use the average $\bar{\lambda}$ of λ_T and λ_I as our estimate of the mean free path.

The estimated absorption is $A = 1 - e^{-\sum_i l_i/\bar{\lambda}_i} \sim 8\%$ where l_i is the thickness of each material in the proton's path. The collision and interaction lengths were taken from the PDG [40].

The proton absorption estimated using the mean-free-path was validated by comparing the charge-normalized coincident yield (Y_{coin}) and electron only yield (Y_{sing}), recorded in the HMS for hydrogen elastic, $H^1(e, e'p)$ runs. The Y_{sing} was obtained for a small central region of HMS acceptance along with tight limits on the invariant mass W ensuring a clean sample of electrons that participated in elastic scattering. While Y_{coin} also obtained with the same tight limits on the HMS acceptance provides the "true" yield where the expected proton from the elastic scattering was also detected. The proton absorption, given by $A = 1 - Y_{coin}/Y_{sing}$, is the fraction of events where an elastic electron event in the HMS did not produce a corresponding proton in the SHMS. Using the $Q^2\!=\!11.5\,(\mathrm{GeV}/c)^2$ data, we estimate a proton absorption of $A = 9.03 \pm 0.71\%$. The uncertainty quoted here is the quadrature sum of the statistical uncertainty and a systematic uncertainty estimated by varying the cuts used to calculate yields. The two methods used to estimate the proton absorption are consistent with each other within uncertainties. The comparison of the two methods determined the overall systematic uncertainty due to the proton absorption quoted in Table III.

I. Systematic Uncertainty

The sources of the systematic uncertainties are categorized into two sources: Q^2-dependent uncertainty (which includes uncertainty due to spectrometer acceptance, event selection, tracking efficiency, radiative corrections, live time and detector efficiency) and normalization uncertainty (which includes uncertainty due to the free cross-section, target thickness, beam charge, and proton absorption). Table III lists the major sources of systematic uncertainties, and the sum in quadrature of these two sets of uncertainties is 4.0%. Since $\mathbf{p}_m$ relies on the momentum and the angle reconstruction for both of the spectrometers, this is the most sensitive variable to validate the quality of the spectrometer acceptance model. The acceptance uncertainty was determined by quantifying the differences in the shape of the $\mathbf{p}_m$ distribution between data and SIMC, and was found to be $\sim 2.6\%$. The systematic uncertainty arising from the cut dependence of the experimental yield was determined by varying the cuts one at a time and recording the variation in yields for the different kinematic settings and the targets. The quadrature sum of the variation over all the different cuts was used as the event selection uncertainty, which we determined to be 1.4%. The tracking efficiency was continuously monitored with an uncertainty of about 0.1% for the HMS and < 0.5% for the SHMS. The uncertainty in the tracking efficiency was obtained from the average variation of the SHMS tracking efficiency when using the three independent criteria for determining the efficiency. The uncertainty due to the radiative correction was estimated by comparing the tail of the missing energy spectra from the 1.5% radiation lengths ^{12}C data, and varying the E_m cut. The measured *ep* elastic cross-section with the hydrogen target, with the background from the aluminum foils subtracted, agrees with the world data, and a comparison to a Monte Carlo simulation yields an overall normalization uncertainty of 1.8%.

TABLE III. Systematic Uncertainties

Source	Q^2 dependent uncertainty (%)
Spectrometer acceptance	2.6
Event selection	1.4
Tracking efficiency	0.5
Radiative corrections	1.0
Live time & Detector efficiency	0.5
Source	**Normalization uncertainty (%)**
Elastic *ep* cross-section	1.8
Target thickness	0.5
Beam charge	1.0
Proton absorption	1.2
Total	4.0

The thickness of the carbon foils was measured to be better than 0.5%, and it is taken as the systematic uncertainty due to target thickness. The variation in the charge-normalized experimental yield was <1% when using all events with beam current above 5 μA or a more restrictive cut of $\pm 3\,\mu$A around the average current (for each interval with stable current). This validates the $\sim 1\%$ uncertainty assigned to the beam charge measurement. The 1.2% uncertainty due to proton absorption was estimated by comparing the two methods used to estimate the proton absorption as described in Sec. III H.

IV. RESULTS

A. Hydrogen elastics

The elastic scattering reaction from the hydrogen target, H$(e, e'p)$, was used to fully constrain the reconstruction spectrometer optics models, to fully understand detector efficiencies, and to determine the overall normalized charge yield. This experiment was a commissioning experiment for the SHMS spectrometer in addition to the HMS spectrometer being run at high central momenta where magnet saturation effects become apparent. In elastic *ep* scattering, the reconstructed W is most sensitive to the electron kinematics. The missing energy and missing momentum are strongly correlated to the proton kinematics. As the HMS was the most well-understood of the two spectrometers, the offset in the central momentum and angle is primarily accounted for by the offset in the reconstructed W. Accounting for these offsets aligns the W peak position for all kinematic settings. The HMS central momentum was determined to saturate by as much as 0.4% at the highest central momentum.

Offsets in the central momentum and optics of the SHMS were improved by studying the focal plane dependencies of the residual difference of the reconstructed missing energy and the missing energy as calculated without the proton information. From simulations with distorted optics, it was observed that first order matrix element corrections were sufficient to remove the dependency of such residuals and was consistent with the offset of the magnet tune mis-sets.

The measured hydrogen data yields were used to determine how well the overall normalization of the data was understood. The cuts on the missing energy and missing momentum on the elastic hydrogen data were varied from 40 to 80 MeV/c. The average deviation in the correct charge yield ratio taken with respect to the simulation yield was determined to be no greater than 1%.

The reconstructed W and missing energy for hydrogen scattering is shown in Fig. 6 for the $Q^2 = 8\,(\mathrm{GeV}/c)^2$ kinematic setting. The reconstruction and resolution of the electron arm (HMS) most significantly contributes to the reconstructed W, while the proton arm (SHMS) dominates the reconstructed missing energy. Some additional resolution effects can be observed in the widths of the distributions relative to the simulated spectra. The reconstructed W and missing energy peak locations show generally good agreement with simulation, and the high missing energy tail agrees well with simulation where contributions due to radiative effects are dominant.

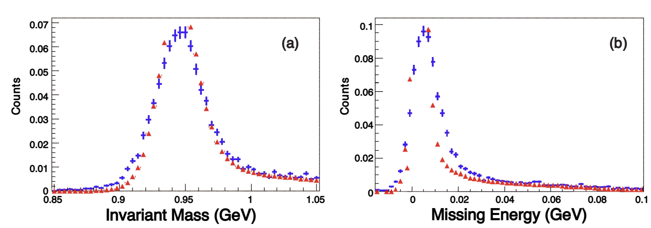

FIG. 6. The comparison between simulation and data (for arbitrary normalization) is shown for the $Q^2 = 8\,(\mathrm{GeV}/c)^2$ setting. The reconstructed W (a) is primarily driven by the electron arm (HMS) reconstruction, while the missing energy (b) is dominated by the proton arm (SHMS).

In the final analysis, the ratio between the measured hydrogen elastic yields was compared to the yields expected from simulation for E_m and $p_\mathrm{m} < 65\,\mathrm{MeV}/c$. When varying this cut in increments of 5 MeV/c from

40–80 MeV/c, the average deviation of the yields at each setting was found to be no greater than 1%. A comparison between the yields at the $Q^2 = 9.5\,(\mathrm{GeV}/c)^2$ setting when the small and large collimators were used indicated a maximum deviation of 1.5% between the yields. These uncertainties, combined, account for a 1.8% uncertainty total on the measured hydrogen elastic cross-section. The hydrogen elastic yield was flat across the four kinematic settings, with a ratio of unity with respect to the simulation.

B. Transparencies

In constructing the transparency, the ratio of the carbon yield is compared to the yield predicted from simulation. The carbon yield in data is first corrected for the detector related inefficiencies. The PWIA simulation is used to construct the denominator in the transparency calculation.

The carbon yields in both data and simulation were cut at $E_\mathrm{m} < 0.08$ GeV and $p_\mathrm{m} < 0.3$ MeV/c. For these cuts in carbon, the effect of nucleon-nucleon (NN) short-range correlations was previously determined to shift the single particle strength to higher p_m, requiring a correction factor to be applied to the data (same factor for all kinematic settings) of 1.11 ± 0.03 [33]. This cut and the corresponding correction factor were used in the previous experiments and are independent of Q^2. The total model-dependent uncertainty of 3.9% is inclusive of the uncertainty in the spectral function (2.8%) and the nucleon-nucleon correlation effects [33].

The full simulated yield is calculated for the same phase-space volume as the experiment. The carbon transparency was observed to be independent of Q^2 from 8–14.2 $(\mathrm{GeV}/c)^2$.

C. Nuclear shell dependent transparency

In the $^{12}C(e, e'p)$ reaction, the protons knocked out from different nuclear shells (for example the $1s_{1/2}$ and $1p_{3/2}$ shells) are expected to have measurable differences in their propagation through the nuclear medium. These differences arise from the differences in the intrinsic momentum distributions of protons occupying different nuclear shells, the differences in quenching of the nuclear shell occupation probabilities, and the presence of a hole around the struck proton due to short-range NN repulsion [42]. These effects should lead to differences in the measured nuclear transparency. In addition, Frankfurt *et al.* [42] suggests that the reduction of FSI (i.e. the CT effect) is more prominent for the $1s_{1/2}$ protons than in $1p_{3/2}$ protons due to differences in the soft re-scattering contributions to the hole excitation. They conclude that it may be advantageous to measure the ratio of the nuclear transparency of protons knocked out of the $1s_{1/2}$ and $1p_{3/2}$ shells, as many experimental errors and theoretical uncertainties are likely to cancel out, making the ratio a more sensitive probe of CT.

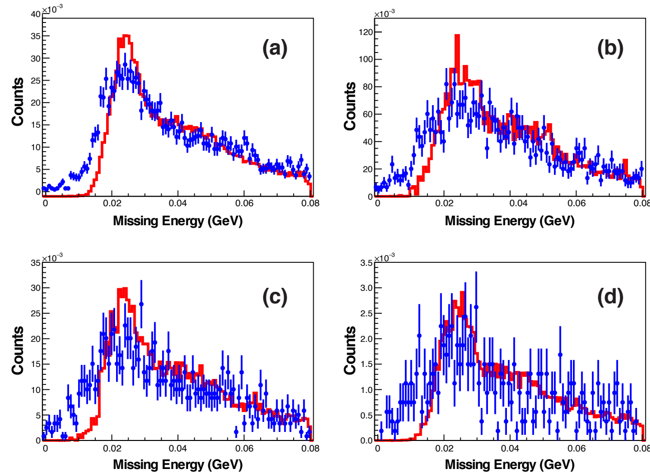

FIG. 7. Carbon missing energy spectrum for the experiment data (blue points) for each of the 4 kinematics, (a) 8, (b) 9.4, (c) 11.4, and (d) 14.4 $(\mathrm{GeV}/c)^2$ and simulated data for the corresponding kinematics (red line). The $1s_{1/2}$ shell and $1p_{3/2}$ shell regions are not clearly separable in the CT data, as compared to the distributions in Ref. [41] because of the poor spectrometer resolution at the high particle momenta.

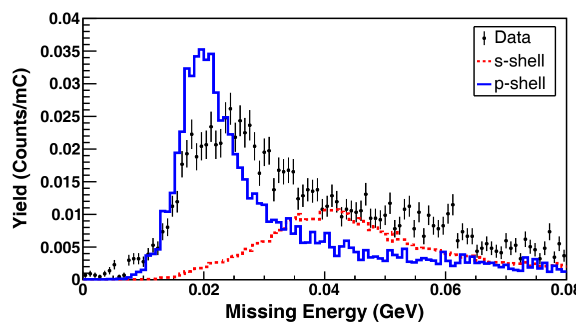

FIG. 8. The solid blue (dashed red) distribution is the simulated $1s_{1/2}$ ($1p_{3/2}$) shell contribution. The black points with error bars (statistical only) are the data distribution from the corresponding $Q^2 = 8\,(\mathrm{GeV}/c)^2$ kinematics.

In order to distinguish the $1s_{1/2}$ shell and $1p_{3/2}$ shell protons (higher and lower excitation energy respectively), the data (blue) are shown as a function of the missing energy in Fig. 7 for each kinematic setting. Also shown are the simulated (red) missing energy distributions. From Fig. 7, the reconstructed missing energy resolution is insufficient at these high Q^2 kinematics (due to the resolution of the high momentum protons) to cleanly separate the $1s_{1/2}$ and $1p_{3/2}$ shell contributions. Therefore, instead of using a single excitation energy to separate the different shell contributions, we have adopted a simulation driven method. The simulated contributions from the $1s_{1/2}$ and $1p_{3/2}$ shells are shown sepa-

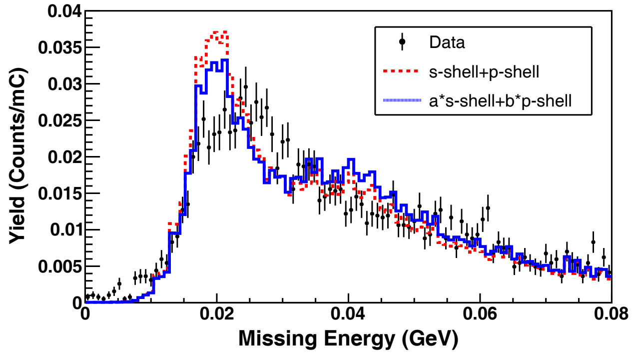

FIG. 9. The dashed red distribution is the nominal sum of $1s_{1/2}$ shell and $1p_{3/2}$ contributions, the solid blue distribution is the $a\,(1s_{1/2}) + b\,(1p_{3/2})$ distribution for best fit to the data as described in the text. The black points with error bars are the data (statistical errors only). All the distributions correspond to $Q^2 = 8\,(\mathrm{GeV}/c)^2$ kinematics.

rately in Figs. 8 along with the data. The nominal sum of the $1s_{1/2}$ and $1p_{3/2}$ contributions (red dashed distribution) compared to data (black distribution with error bars) is shown in Fig. 9. The simulation uses the constraint that the carbon nucleus has 2 protons in the $1s_{1/2}$ shell, and 4 protons in the $1p_{3/2}$ shell. The simulated $1s_{1/2}$ and $1p_{3/2}$ shell spectra were then parameterized as $a\,(1s_{1/2}) + b\,(1p_{3/2})$, and the best values for the parameters a and b were obtained from a fit to the measured yield. The combined distribution for the parameters obtained from the best fit to the data is shown as the blue solid distribution in Fig. 9.

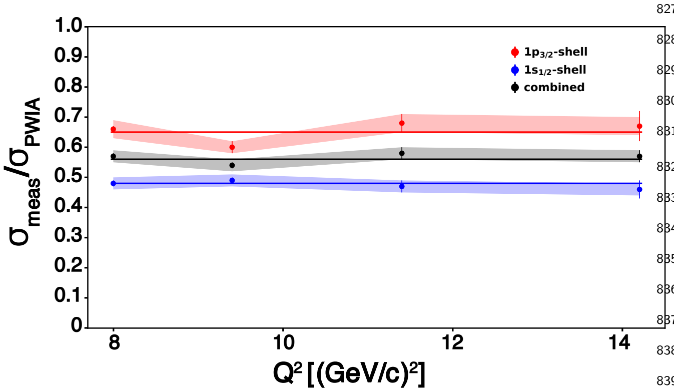

FIG. 10. $1s_{1/2}$ (blue circles) and $1p_{3/2}$ shells (red squares) transparency as a function of Q^2. The combined transparency is shown by black triangles. The straight lines are fit to a constant value for the respective shells. The error bars on each point show the statistical uncertainty while the bands represent the total systematic uncertainty of the $1p_{3/2}$ shell (red), $1s_{1/2}$ shell (blue), and the total (black) transparencies.

The nuclear transparency of the $1s_{1/2}$ and $1p_{3/2}$ shell protons is obtained from the product of the measured

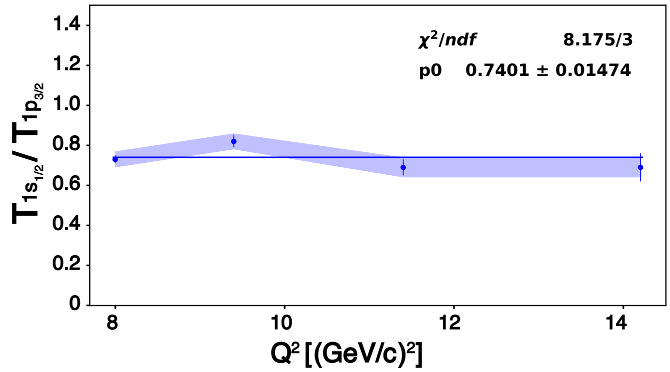

FIG. 11. The ratio of transparencies for the $1s_{1/2}$ shell to the $1p_{3/2}$ shell protons as a function of Q^2. The error bars show the statistical uncertainty, while the band represents the total systematic uncertainty. The solid line shows the fit of the data to a polynomial of grade 0.

combined transparency with the two parameters a and b which give the best data-driven value of the relative proportion of $1s_{1/2}$ and $1p_{3/2}$ shell strength. The $1s_{1/2}$ and $1p_{3/2}$ shell transparencies for each Q^2 are listed in Table IV. The total systematic uncertainty for $1s_{1/2}$ and $1p_{3/2}$ shell transparencies include the uncertainty of the fit parameters and are summarized in Table IV.

The shell-dependent transparency as a function of Q^2 is shown in the Fig. 10. The blue and the red bands are the systematic uncertainties, which are the quadrature sum of the 4% systematic uncertainty and the uncertainty of determining the $1s_{1/2}$ shell and $1p_{3/2}$ shell transparencies separately (obtained from the fit to data). The black band in the combined transparency is the total systematic uncertainty of 4%. The shell-dependent and combined transparency were also fit to a constant value, with the fit parameters and the quality of the fits listed in Table V. The shell-dependent nuclear transparency does not show any variation with Q^2.

The ratio of the nuclear transparency from $1s_{1/2}$ to $1p_{3/2}$ shell is shown in Fig. 11. The differences between the $1s_{1/2}$ and $1p_{3/2}$ shell transparencies arise from the differences in the momentum distributions, excitation energy and differences in the re-distribution of strength due to nucleons in short-range correlations, radiative effects and the presence of a hole around the struck proton due to short-range NN repulsion. According to Frankfurt *et al.* [42], the $1s_{1/2}$ shell is expected to show a larger change due to CT than $1p_{3/2}$ shell. The possible cancellation of experimental and theoretical uncertainties makes the ratio of the $1s_{1/2}$ to $1p_{3/2}$ shell transparencies a more sensitive observable of CT compared to the transparency averaged over the two shells. The onset of CT would be observed as an increase in the ratio with increasing Q^2. However, as can be seen in Fig. 11, the transparency ratio is independent of Q^2 reinforcing the observed lack of CT-like effects at the kinematics probed in this experiment.

TABLE IV. The $1s_{1/2}$ and $1p_{3/2}$ shell transparencies for the ^{12}C nucleus along with statistical, systematic and total uncertainties.

Q^2	$1s_{1/2}$				$1p_{3/2}$			
$(\mathrm{GeV}/c)^2$	Transparency (T)	Statistical error	Systematic error	Total %	Transparency (T)	Statistical error	Systematic error	Total %
8.0	0.48	0.01	0.02	4.122	0.66	0.01	0.02	4.007
9.4	0.49	0.01	0.02	4.007	0.60	0.02	0.02	4.009
11.4	0.47	0.02	0.02	4.902	0.68	0.03	0.03	4.000
14.2	0.46	0.03	0.02	4.551	0.67	0.05	0.02	4.583

TABLE V. Results of the fit to a constant transparency as a function of Q^2 for the combined, $1p_{3/2}$ and $1s_{1/2}$ shells transparencies.

Fit result	combined	$1p_{3/2}$ shell	$1s_{1/2}$ shell
χ^2/df	2.08	2.80	0.53
T_{fit}	0.56±0.01	0.65±0.01	0.48±0.01

D. Asymmetry of the missing momentum distribution

In parallel kinematics under the PWIA, the distribution of events with the missing momentum $\vec{p}_m$ parallel (negative) and anti-parallel (positive) to the direction of momentum transfer $\vec{q}$ are symmetric. The differences in the experimental acceptance for negative and positive p_m give rise to most of the asymmetry that is observed in the missing momentum spectrum as shown in Fig. 12. A small fraction of the asymmetry is due to the small but finite angular coverage of protons on the left and right side of $\vec{q}$. This left-right asymmetry is modified by FSI mechanisms beyond the impulse approximation including Meson Exchange currents (MEC) and Isobar configurations (IC) [43, 44]. Further, it was suggested that the Fermi motion of bound nucleons may be a source of CT in quasielastic scattering, particularly when the initial momentum of the bound nucleon is in the direction opposite to the $\vec{q}$ [45]. This implies that CT effects are highly dependent on the sign of p_m [46]. This is because all the excited baryon states are produced preferentially at positive p_m, and therefore, it is more probable to realize a point-like-state for positive p_m. Therefore, it is interesting to measure the Q^2 dependence of the missing momentum asymmetry. This asymmetry, A_{p_m}, can be quantified as

$$A_{p_m} = \frac{N_+ - N_-}{N_+ + N_-} \tag{3}$$

with N_+ being the number of events integrated over a fixed range of positive p_m and N_- being the number of events integrated over the same range of negative p_m. The range of $|p_m|$ is chosen appropriately to exclude the regions where the impulse approximation is invalid and could influence the asymmetry from sources other than quasi-elastic scattering.

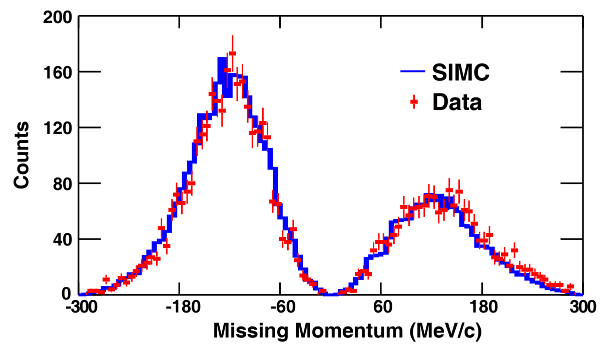

FIG. 12. The missing momentum distribution is shown for the kinematic setting at $Q^2 = 8$ $(\mathrm{GeV}/c)^2$. The data (red) is well reproduced by the PWIA simulated spectrum (blue).

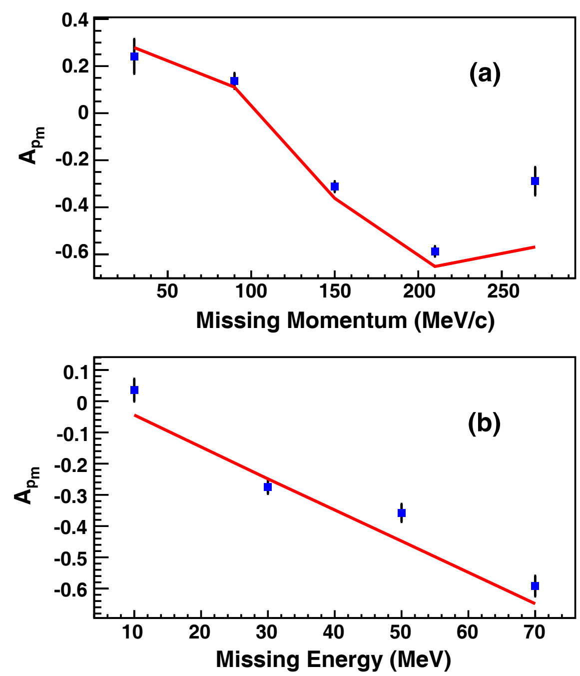

FIG. 13. Left-right asymmetry as a function of the missing momentum (a) and missing energy (b) for $Q^2 = 8.0\,(\mathrm{GeV}/c)^2$. The red line indicates the simulation data for the corresponding points.

The PWIA simulation (blue) of the experiment can describe the $\vec{p}_m$ asymmetry very well as seen in Fig. 12. This is further illustrated in Fig. 13 which shows the calculated A_{p_m} as a function of the missing momentum (top) and the missing energy (bottom) for the Q^2 = 8.0 (GeV/c)^2 kinematic setting. The increase of $|A_{p_m}|$ with respect to E_m and $|p_m|$ is as expected from the PWIA simulation (solid red lines). The small deviation at the highest missing momentum bin may be due to MEC that are not included in the simulation [43]. In the presence of additional FSI, such as when measuring in perpendicular kinematics, the $|A_{p_m}|$ is known to decrease significantly relative to the PWIA expectation with increasing E_m and $|p_m|$ [44]. Thus, measurements of A_{p_m} in perpendicular kinematics could prove to be better probes of CT effects in future experiments. The signature of CT in such an experiment would be an increase in A_{p_m} as a function of Q^2. Finally, Fig. 14 shows the ratio of the measured A_{p_m} asymmetry to the calculated asymmetry from the PWIA simulation as a function of Q^2. A range of $|p_m| < 300$ MeV/c was used to extract the A_{p_m} for all four Q^2 settings. The Q^2 independence of the ratio indicates good agreement between the data and the PWIA simulation. The agreement between the measured and PWIA values of A_{p_m} in parallel kinematics indicates the lack of CT-like effects or any additional FSI beyond the impulse approximation for the kinematics probed in this experiment.

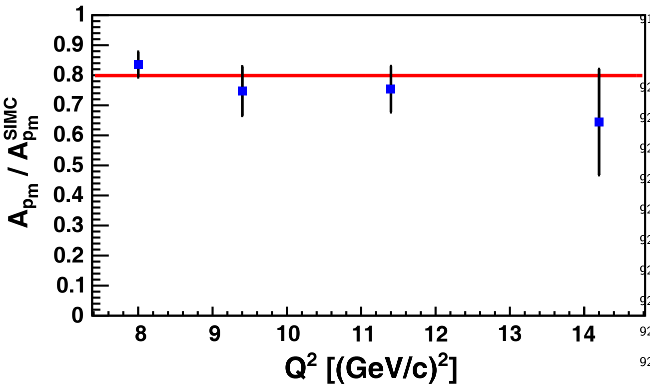

FIG. 14. The ratio of the A_{p_m} asymmetry in data to simulation as a function of the kinematics settings used in the experiment. The red line is the constant fit to the data.

V. CONCLUSIONS

Using the upgraded 12 GeV CEBAF beam at JLab, coincidence $(e, e'p)$ data were collected with ^1H and ^{12}C targets for Q^2 values between 8 and 14.2 (GeV/c)^2. The Nuclear transparency was extracted at each of the four kinematic settings by integrating the charge-normalized yields and taking their ratio with the yields from a PWIA simulation of the experiment. The transparency measured at the lowest kinematic point at $Q^2 = 8$ (GeV/c)^2 agrees with prior measurements at JLab. The Q^2 independence of the measured transparencies is consistent with traditional Glauber multiple scattering theory and does not show an onset of color transparency in $^{12}C(e, e'p)$ below $Q^2 = 14.2$ (GeV/c)^2. We have also extracted the nuclear transparency of the $1s_{1/2}$ and $1p_{3/2}$ shell protons in ^{12}C and their ratio. All of these observables show a Q^2 independence that rules out observation of the onset of CT for protons up to Q^2 of 14.2 (GeV/c)^2 in $^{12}C(e, e'p)$. We have also extracted the asymmetry of the $^{12}C(e, e'p)$ events along and opposite to the momentum transfer $\vec{q}$ in parallel kinematics. The measured asymmetry is consistent with the expectations from a PWIA simulation of the experiment. These results rule out any additional reaction mechanisms such as CT for $^{12}C(e, e'p)$ in parallel kinematics.

VI. ACKNOWLEDGMENTS

This work was funded in part by the U.S. Department of Energy, including contract AC05-06OR23177 under which Jefferson Science Associates, LLC operates Thomas Jefferson National Accelerator Facility, and by the U.S. National Science Foundation and the Natural Sciences and Engineering Research Council of Canada. We wish to thank the staff of Jefferson Lab for their vital support throughout the experiment. We are also grateful to all granting agencies providing funding support to authors throughout this project.

[1] A. H. Mueller (Les Arcs, France, 1983).
[2] S. J. Brodsky, G. T. Bodwin, and G. Lepage, in *XIII International Symposium on Multiparticle Dynamics* (1982) pp. 841–854.
[3] D. Perkins, Phil. Mag. **46**, 1146 (1955).
[4] J. Iwadare, The Philosophical Magazine: A Journal of Theoretical Experimental and Applied Physics **3**, 680 (1958), https://doi.org/10.1080/14786435808237003.
[5] L. El-Fassi *et al.*, Phys. Lett. B **712**, 326 (2012).
[6] B. Clasie *et al.*, Phys. Rev. Lett. **99**, 242502 (2007).
[7] X. Qian *et al.*, Phys Rev. C **81**, 055209 (2010).
[8] D. Dutta *et al.*, Phys. Rev. C **68**, 021001R (2003).
[9] K. Ackerstaff *et al.* (HERMES), Phys. Rev. Lett. **82**, 3025 (1999), arXiv:hep-ex/9811011.
[10] M. Arneodo *et al.* (New Muon), Nucl. Phys. B **429**, 503 (1994).
[11] A. Carroll *et al.*, Phys. Rev. Lett. **61**, 1698 (1988).
[12] I. Mardor *et al.*, Phys. Rev. Lett. **81**, 5085 (1998).
[13] A. Leksanov *et al.*, Phys.Rev.Lett. **87**, 212301 (2001), arXiv:hep-ex/0104039.

[14] B. Kundu, J. Samuelsson, P. Jain, and J. P. Ralston, Phys. Rev. D **62**, 113009 (2000).

[15] S. J. Brodsky and G. F. de Teramond, Phys Rev. Lett. **60**, 1924 (1988).

[16] V. R. Pandharipande and S. C. Pieper, Phys. Rev. C **45**, 791 (1992).

[17] D. Dutta *et al.*, "The Search for Color Transparency at 12 GeV," Jefferson Lab experiment E12-06-107.

[18] D. Bhetuwal, J. Matter, H. Szumila-Vance, M. L. Kabir, D. Dutta, R. Ent, *et al.* (Jefferson Lab Hall C Collaboration), Phys. Rev. Lett. **126**, 082301 (2021).

[19] K. Garrow *et al.*, Phys. Rev. C **66**, 044613 (2002).

[20] J. Aclander *et al.*, Phys. Rev. C **70**, 015208 (2004).

[21] L. Harwood, in *Proceedings NA-PAC2013*.

[22] T. H. spectrometer in Hall-C, *HMS Spectrometer*.

[23] D. Abbott *et al.*, Phys. Rev. Lett. **80**, 5072 (1998).

[24] T. S. spectrometer in Hall-C, *publication in preparation*.

[25] D. Bhetuwal, *Nuclear Transparency from Quasi-elastic $^{12}C(e,e'p)$ scattering reaction up to $Q^2 = 14.2\ (GeV/c)^2$ in Hall C at Jefferson Lab*, Ph.D. thesis, Mississippi State University (unpublished) (2021), https://misportal.jlab.org/ul/generic_reports/hc_thesis.cfm.

[26] C. Yero, *Cross Section Measurements of Deuteron Electro-Disintegration at Very High Recoil Momenta and Large 4-Momentum Transfers* (Q^2), Ph.D. thesis, Florida International University (unpublished) (2020), https://misportal.jlab.org/ul/publications/view_pub.cfm?pub_id=16338.

[27] J. Matter, *Ruling Out the Onset of Color Transparency Below (Q^2)=14.2 GeV^2 in Quasielastic $^{12}C(e,e'p)$ Scateering*, Ph.D. thesis, University of Virginia (unpublished) (2021), https://misportal.jlab.org/ul/generic_reports/hc_thesis.cfm.

[28] V. Klioukhine, DSM/DAPNIA/STCM Technical Report 5C 2100T-M 1000 **020** (1997).

[29] M. Berz and K. Makino, (2006).

[30] W. H. Press, S. A. Teukolsky, W. T. Vetterling, and B. P. Flannery, *Numerical Recipes 3rd Edition: The Art of Scientific Computing*, 3rd ed. (Cambridge University Press, 2007).

[31] https://hallcweb.jlab.org/simc/.

[32] T. De Forest, Nucl. Phys. A **392**, 232 (1983).

[33] N. C. R. Makins *et al.*, Phys. Rev. Lett **72**, 1986 (1994).

[34] S. Pollock, H. W. L. Naus, and J. H. Koch, Phys. Rev. C **53**, 2304 (1996).

[35] T. De Forest, Nuclear Physics A **392**, 232 (1983).

[36] T. G. O'Neill *et al.*, Phys. Lett. **351**, 87 (1995).

[37] D. Abbott *et al.*, Phys. Rev. Lett. **80**, 5072 (1998).

[38] L. W. Mo and Y. S. Tsai, Rev. Mod. Phys. **41**, 205 (1969).

[39] R. Ent, B. W. Filippone, N. C. R. Makins, R. G. Milner, T. G. O'Neill, and D. A. Wasson, Phys. Rev. C **54**, 054610 (2001).

[40] D. Groom, "Atomic Nuclear Properties," (2011), https://pdg.lbl.gov/2018/AtomicNuclearProperties/.

[41] D. Izraeli, T. Brecelj, P. Achenbach, A. Ashkenazi, R. Böhm, E. Cohen, M. Distler, A. Esser, R. Gilman, T. Kolar, *et al.*, Physics Letters B **781**, 95 (2018).

[42] L. Frankfurt, M. Strikman, and M. Zhalov, Nuclear Physics A **515**, 599 (1990).

[43] K. G. Fissum, M. Liang, *et al.* (Jefferson Lab Hall A Collaboration), Phys. Rev. C **70**, 034606 (2004).

[44] J. M. Udias, J. A. Caballero, E. Moya de Guerra, J. E. Amaro, and T. W. Donnelly, Phys. Rev. Lett. **83**, 5451 (1999).

[45] B. Jennings and B. Kopeliovich, Phys. Rev. Lett. **70**, 3384 (1993).

[46] A. Bianconi, S. Boffi, and D. E. Kharzeev, Phys. Lett. B **325**, 294 (1994), arXiv:nucl-th/9310012.